Wide-Field Lensing Mass Maps from DES Science Verification Data

V. Vikram,[1,2] C. Chang,[3]* B. Jain,[2] D. Bacon,[4] A. Amara,[3] M. Becker,[5,6]
G. Bernstein,[2] C. Bonnett,[7] S. Bridle,[8] D. Brout,[2] M. Busha,[5,6] J. Frieman,[9,10]
E. Gaztanaga,[11] W. Hartley,[3] M. Jarvis,[2] T. Kacprzak,[3] O. Lahav,[12] B. Leistedt,[12]
H. Lin,[10] P. Melchior,[13,14] H. Peiris,[12] E. Rozo,[15] E. Rykoff,[6,16] C. Sánchez, [7]
E. Sheldon,[17] M. Troxel,[8] R. Wechsler,[5,6,16] J. Zuntz,[8] T. Abbott,[18] F. B. Abdalla,[12]
R. Armstrong,[2] M. Banerji,[19,20] A. H. Bauer,[11] A. Benoit-Lévy,[12] E. Bertin,[21]
D. Brooks,[12] E. Buckley-Geer,[10] D. L. Burke,[6,16] D. Capozzi,[4] A. Carnero Rosell,[22,23]
M. Carrasco Kind,[24,25] F. J. Castander,[11] M. Crocce, [11] C. B. D'Andrea,[4]
L. N. da Costa,[22,23] D. L. DePoy,[26] S. Desai,[27] H. T. Diehl,[10] J. P. Dietrich,[27,28]
C. E Cunha,[29] J. Estrada,[10] A. E. Evrard,[30] A. Fausti Neto,[22] E. Fernandez,[7]
B. Flaugher,[10] P. Fosalba,[11] D. Gerdes,[30] D. Gruen,[31,32] R. A. Gruendl,[24,25]
K. Honscheid,[13,14] D. James,[18] S. Kent,[10] K. Kuehn,[33] N. Kuropatkin,[10] T. S. Li,[26]
M. A. G. Maia,[22,23] M. Makler,[34] M. March,[2] J. Marshall,[26] Paul Martini,[13,14]
K. W. Merritt,[10] C. J. Miller,[30,35] R. Miquel,[7,36] E. Neilsen,[10] R. C. Nichol,[4] B. Nord,[10]
R. Ogando,[22,23] A. A. Plazas,[17,37] A. K. Romer,[38] A. Roodman,[7,16] E. Sanchez,[39]
V. Scarpine,[10] I. Sevilla,[24,39] R. C. Smith,[18] M. Soares-Santos,[10] F. Sobreira,[10,22]
E. Suchyta,[13,14] M. E. C. Swanson,[25] G. Tarle,[27] J. Thaler,[24] D. Thomas,[4,40]
A. R. Walker,[18] J. Weller[27,28,31]

e-mail address: chihway.chang@phys.ethz.ch

12 April 2015

ABSTRACT

Weak gravitational lensing allows one to reconstruct the spatial distribution of the projected mass density across the sky. These "mass maps" provide a powerful tool for studying cosmology as they probe both luminous and dark matter. In this paper, we present a weak lensing mass map reconstructed from shear measurements in a 139 deg^2 area from the Dark Energy Survey (DES) Science Verification (SV) data overlapping with the South Pole Telescope survey. We compare the distribution of mass with that of the foreground distribution of galaxies and clusters. The overdensities in the reconstructed map correlate well with the distribution of optically detected clusters. Cross-correlating the mass map with the foreground galaxies from the same DES SV data gives results consistent with mock catalogs that include the primary sources of statistical uncertainties in the galaxy, lensing, and photo-z catalogs. The statistical significance of the cross-correlation is at the 6.8σ level with 20 arcminute smoothing. A major goal of this study is to investigate systematic effects arising from a variety of sources, including PSF and photo-z uncertainties. We make maps derived from twenty variables that may characterize systematics and find the principal components. We find that the contribution of systematics to the lensing mass maps is generally within measurement uncertainties. We test and validate our results with mock catalogs from N-body simulations. In this work, we analyze less than 3 % of the final area that will be mapped by the DES; the tools and analysis techniques developed in this paper can be applied to forthcoming larger datasets from the survey.

1 INTRODUCTION

Weak gravitational lensing is a powerful tool for cosmological studies (see Bartelmann & Schneider 2001; Hoekstra & Jain 2008, for detailed reviews). As light from distant galaxies passes through the mass distribution in the Universe, its trajectory gets perturbed, causing the apparent galaxy shapes to be distorted. Weak lensing statistically measures this small distortion, or "shear", for a large number of galaxies to infer the 3D matter distribution. This allows us to constrain cosmological parameters and study the distribution of mass in the Universe.

Since its first discovery, the accuracy and statistical precision of weak lensing measurements have improved significantly (Van Waerbeke et al. 2000; Kaiser, Wilson & Luppino 2000; Bacon, Refregier & Ellis 2000; Hoekstra et al. 2006; Lin et al. 2012; Heymans et al. 2012). Most of these previous studies constrain cosmology through N-point statistics of the shear signal (*e.g.* Bacon et al. 2003; Jarvis et al. 2006; Semboloni et al. 2006; Fu et al. 2014; Jee et al. 2013; Kilbinger et al. 2013). In this paper, however, we focus on generating two-dimensional wide-field projected mass maps from the measured shear (Van Waerbeke, Hinshaw & Murray 2014). These mass maps are particularly useful for viewing the non-Gaussian distribution of dark matter in a different way than is possible with N-point statistics.

Probing the dark matter distribution in the Universe is particularly important for several reasons. Based on the peak statistics from a mass map it is possible to identify dark matter halos and constrain cosmological parameters (*e.g.* Jain & Van Waerbeke 2000; Fosalba et al. 2008; Kratochvil, Haiman & May 2010; Bergé, Amara & Réfrégier 2010). Mass maps also allow us to study the connection between baryonic matter (both in stellar and gaseous forms) and dark matter (Van Waerbeke, Hinshaw & Murray 2014). This can be measured by cross correlating light maps and gas maps with weak lensing mass maps. Correlation with light maps, which can be constructed using observed galaxies, groups and clusters of galaxies etc., can be used to constrain galaxy bias, the mass-to-light ratio, and the dependence of these statistics on redshift and environment (Amara et al. 2012; Jauzac et al. 2012; Shan et al. 2014; Hwang et al. 2014). However, one needs to take caution when interpreting the weak lensing mass maps, as the completeness and purity of structure detection via these maps is not very high due to their noisy nature (White, van Waerbeke & Mackey 2002).

One other interesting application of the mass map is that it allows us to identify large scale structures (both super-clusters and voids) which are otherwise difficult to find (*e.g.* Heymans et al. 2008). Characterizing the statistics of large structures can be a sensitive probe of cosmological models. Structures with masses as high or higher than clusters require special attention as the massive end of the halo mass function is very sensitive to the cosmology (Bahcall & Fan 1998; Haiman, Mohr & Holder 2001; Holder, Haiman & Mohr 2001). These rare structures also allows us to constrain different theories of gravity (Knox, Song & Tyson 2006; Jain & Khoury 2010). In addition to the study of the largest assemblies of mass, the study of number density of the largest voids allows further tests of the ΛCDM model (*e.g.* Plionis & Basilakos 2002).

Similar mass mapping technique as used in this paper has been previously applied to the Canada-France-Hawaii Telescope Lensing Survey (CFHTLenS) as presented in Van Waerbeke et al. (2013). Their work demonstrated the potential scientific value of these wide-field lensing mass maps, including measuring high-order moments of the maps and cross-correlation with galaxy densities. The total area of the mass map in that work is similar to our dataset, though it was divided into four separate smaller fields.

The main goal of this paper is to construct a weak lensing mass map from a 139 deg² area in the Dark Energy Survey[1] (DES, The Dark Energy Survey Collaboration 2005; Flaugher 2005) Science Verification (SV) data, which overlaps with the South Pole Telescope survey (the SPT-E field). The SV data were recorded using the newly commissioned wide-field mosaic camera, the Dark Energy Camera (DECam; Diehl & Dark Energy Survey Collaboration 2012; Flaugher et al. 2012; Flaugher & The Dark Energy Survey Collaboration submitted to A. J.) on the 4m Blanco telescope at the Cerro Tololo Inter-American Observatory (CTIO) in Chile. We cross correlate this reconstructed mass map with optically identified structures such as galaxies and clusters of galaxies. This work opens up several directions for future explorations with these mass maps.

This paper is organized as follows. In §2 we describe the theoretical foundation and methodology for constructing the mass maps and galaxy density maps used in this paper. We then describe in §3 the DES dataset used in this work, together with the simulation used to interpret our results. In §4 we present the reconstructed mass maps and discuss qualitatively the correlation of these maps with known foreground structures found via independent optical techniques. In §5, we quantify the wide-field mass-to-light correlation on different spatial scales using the full field. We show that our results are consistent with expectations from simulations. In §6 we estimate the level of contamination by systematics in our results from a wide range of sources. Finally, we conclude in §7.

2 METHODOLOGY

In this section we first briefly review the principles of weak lensing in §2.1. Then, we describe the adopted mass reconstruction method in §2.2. Finally in §2.3, we describe our method of generating galaxy density maps. The galaxy density maps are used as independent mass tracers in this work to help confirm the signal measured in the weak lensing mass maps.

2.1 Weak gravitational lensing

When light from galaxies passes through a foreground mass distribution, the resulting bending of light leads to the galaxy images being distorted (*e.g.* Bartelmann & Schneider 2001). This phenomenon is called gravitational lensing. The local mapping between the source (β) and image (θ) plane coordinates (aside from an overall displacement) can be described by the lens equation:

$$\beta - \beta_0 = A(\theta)(\theta - \theta_0), \qquad (1)$$

where β_0 and θ_0 is the reference point in the source and the image plane. A is the Jacobian of this mapping, given by

$$A(\theta) = (1 - \kappa) \begin{pmatrix} 1 - \mu_1 & -\mu_2 \\ -\mu_2 & 1 + \mu_1 \end{pmatrix}, \qquad (2)$$

where κ is the convergence, $\mu_i = \gamma_i/(1 - \kappa)$ is the reduced shear and γ_i is the shear. $i = 1, 2$ refers to the 2D coordinates in the plane. The premultiplying factor $(1 - \kappa)$ causes galaxy images to be dilated or reduced in size, while the terms in the matrix cause distortion in the image shapes. Under the Born approximation, which

---

[1] http://www.darkenergysurvey.org

assumes that the deflection of the light rays due to the lensing effect is small, A is given by (*e.g.* Bartelmann & Schneider 2001)

$$A_{ij}(\theta, r) = \delta_{ij} - \psi_{,ij}, \tag{3}$$

where ψ is the lensing deflection potential, or projected gravitational potential along the line of sight. For a spatially flat Universe, it is given by the line of sight integral of the 3-dimensional gravitational potential Φ,

$$\psi(\theta, r) = -2 \int_0^r dr' \frac{r - r'}{rr'} \Phi(\theta, r'), \tag{4}$$

where r is the comoving distance. Comparison of Eqn. 3 with Eqn. 2 gives

$$\kappa = \frac{1}{2} \nabla^2 \psi; \tag{5}$$

$$\gamma = \gamma_1 + i\gamma_2 = \frac{1}{2} \left(\psi_{,11} - \psi_{,22} \right) + i\psi_{,12}. \tag{6}$$

For the purpose of this paper, we use the Limber approximation which lets us use the Poisson equation for the density fluctuation $\delta = (\Delta - \bar{\Delta})/\bar{\Delta}$ (where Δ and $\bar{\Delta}$ are the 3-dimensional density and mean density respectively):

$$\nabla^2 \Phi = \frac{3H_0^2 \Omega_m}{2a} \delta, \tag{7}$$

where a is the cosmological scale factor. Equations 4 and 5 give the convergence measured at a sky coordinate θ from sources at comoving distance r:

$$\kappa(\theta, r) = \frac{3H_0^2 \Omega_m}{2c^2} \int_0^r dr' \frac{(r - r')r'}{r} \frac{\delta(\theta, r')}{a(r')}. \tag{8}$$

We can generalize to sources with a distribution in comoving distance (or redshift) $f(r)$ as: $\kappa(\theta) = \int \kappa(\theta, r) f(r) dr$. That is, a κ map constructed over a region on the sky gives us the integrated mass density fluctuation in the foreground of the κ map weighted by the lensing weight $p(r)$, which is itself an integral over $f(r)$:

$$\kappa(\theta) = \frac{3H_0^2 \Omega_m}{2c^2} \int dr p(r) r \frac{\delta(\theta, r)}{a(r)}, \tag{9}$$

with

$$p(r) = \int_r^{r_H} dr' f(r') \frac{r' - r}{r}. \tag{10}$$

where r_H is the comoving distance to the horizon. For a specified cosmological model and $f(r)$ specified by the redshift distribution of source galaxies, the above equations provide the basis for predicting the statistical properties of κ.

2.2 Mass maps from Kaiser-Squires reconstruction

In this paper we perform weak lensing mass reconstruction based on the method developed in Kaiser & Squires (1993). The Kaiser-Squires (KS) method is known to work well up to a constant additive factor as long as the structures are in the linear regime (Van Waerbeke et al. 2013), *i.e.* scales larger than clusters. In the nonlinear regime (scales corresponding to clusters or smaller structures) improved methods have been developed to recover the mass distribution (*e.g.* Bartelmann et al. 1996; Bridle et al. 1998). In this paper we are interested in the mass distribution on large scales; we can therefore restrict ourselves to the KS method. The KS method

works as follows. The Fourier transform of the observed shear, $\hat{\gamma}$, relates to the Fourier transform of the convergence, $\hat{\kappa}$ through

$$\hat{\kappa}_l = D_l^* \hat{\gamma}_l, \tag{11}$$

$$D_l = \frac{l_1^2 - l_2^2 + 2il_1 l_2}{|l|^2}, \tag{12}$$

where l_i are the Fourier counterparts for the angular coordinates θ_i, $i = 1, 2$ represent the two dimensions of sky coordinate. The above equations hold true for $l \neq 0$. In practice we apply a sinusoidal projection of sky with a reference point at RA=71.0 and then pixelize the observed shears with a pixel size of 5 arcmin before Fourier transforming. Given that we mainly focus on scales less than a degree in this paper, the errors due to the projection is small (Van Waerbeke et al. 2013).

The inverse Fourier transform of Eqn. 11 gives the convergence for the observed field in real space. Ideally, the imaginary part of the inverse Fourier transform will be zero as the convergence is a real quantity. However, noise, systematics and masking causes the reconstruction to be imperfect, with non-zero imaginary convergence as we will quantify in §5.2. The real and imaginary parts of the reconstructed convergence are referred to as the E and B-mode κ respectively. In our reconstruction procedure we set shears to zero in the masked regions.

One of the issues with the KS inversion is that the uncertainty in the reconstructed convergence is formally infinite for a discrete set of noisy shear estimates. This is because the statistically uncorrelated ellipticities of galaxies result in a white noise power spectrum which integrates to infinity for large spatial frequencies. Therefore we need to remove the high frequency components by applying a filter. For a Gaussian filter of size σ the covariance of the statistical noise in the convergence map can be written as (Van Waerbeke 2000)

$$\langle \kappa(\theta)\kappa(\theta') \rangle = \frac{\sigma_\varepsilon^2}{4\pi\sigma^2 n_g} \exp\left(-\frac{|\theta - \theta'|^2}{2\sigma^2} \right), \tag{13}$$

where σ_ε is the RMS of the single component ellipticity (which contains the intrinsic shape noise and measurement noise) and n_g is the number density of the source galaxies. Eqn. 13 implies that the shape noise contribution to the convergence map reduces with increasing size of the Gaussian window and number density of the background source galaxies.

2.3 Lensing-weighted galaxy density maps

In addition to the mass map generated from weak lensing measurements in §2.2, we also generate mass maps based on the assumption that galaxies are linearly biased tracers of mass in the foreground. In particular, we study two galaxy samples: the general field galaxies and the Luminous Red Galaxies (LRGs). Properties of the samples used in this work such as the redshift distribution, magnitude distribution etc. are described in §3.2. To compare with the weak lensing mass map, we assume that the bias is constant. However, bias may change with spatial scale, redshift, magnitude and other galaxy properties. This can introduce differences between the weak lensing mass map and foreground map. In this paper we neglect such effects since we mostly focus on large scales where the departures from linear bias are small.

Based on a given sample of mass tracer we generate a weighted foreground map (κ_g) after applying an appropriate lensing weight to each galaxy before pixelation. In principle the weight

increases the signal-to-noise (S/N) of the cross-correlation between the lensing mass map and the foreground density map. The lensing weight (Eqn. 10) depends on the comoving distance to the source and lens, and the distance between them. To generate the weighted galaxy density map, we first generate a three-dimensional grid of the galaxies. We estimate the density contrast in each of these cells as follows:

$$\delta_g^{ijk} = \frac{n_{ijk} - \bar{n}_k}{\bar{n}_k} \qquad (14)$$

where (i, j) is the pixel index in the projected 2D sky and k is the pixel index in the redshift direction. n_{ijk} is the number of galaxies in the ijk^{th} cell and $\bar{n}_k$ is the average number of galaxies per pixel in the kth redshift bin. This three dimensional grid of galaxy density fluctuations will be used to estimate κ_g according to the discrete version of Eqn. 8,

$$\kappa_g^{ij} = \frac{3H_0^2\Omega_m}{2c^2} \sum_k \Delta \frac{\delta_k^{3D} d_k}{a_k} \sum_{l>k} \frac{(d_l - d_k)g_l}{d_l}, \qquad (15)$$

where κ_g^{ij} is the weighted foreground map at the pixel (i, j); k and l represent indices along the redshift direction for lens and source, Δ is the physical size of the redshift bin, d_l is the angular diameter distance to source, g_k is the probability density of the source redshift distribution at redshift l and δ_k^{3D} is the foreground density fluctuation at angular diameter distance d_k. In this work, we adopt the following cosmological parameters: $\Omega_m = 0.3$, $\Omega_\Lambda = 0.7$, $\Omega_k = 0.0$, $h = 0.72$ (Hinshaw et al. 2013). Our results depend very weakly on the exact values of these cosmological parameters.

3   DATA AND SIMULATIONS

The measurements in this paper are based on 139 deg^2 of data in the SPT-E field, observed as part of the Science Verification (SV) data from DES. The SV data were taken during the period of November 2012 – February 2013 before the official start of the science survey. The data were taken shortly after DECam commissioning and were used to test survey operations and assess data quality. Five optical filters ($grizY$) were used throughout the survey, with typical exposure times being 90 sec for $griz$ and 45 sec for Y. The final median depth estimates of this data set in our region of interest are $g \sim 24.0$, $r \sim 23.9$, $i \sim 23.0$ and $z \sim 22.3$.

Below we introduce in §3.1 the relevant data used in this work and in §3.3 the simulations we use to interpret our measurements. Then we define in §3.2 two subsamples of the SV data that we identify as "foreground (lens)" and "background (source)" galaxies for the main analysis of the paper.

3.1   The DES SVA1 Gold galaxy catalogs

All galaxies used for foreground catalogs and lensing measurements are drawn from the DES SVA1 Gold Catalog (Rykoff et al., in preparation) and several extensions to it. The main catalog is a product of the DES Data Management (DESDM) pipeline version "SVA1" (Yanny et al., in preparation). The DESDM pipeline, as described in Ngeow et al. (2006); Sevilla et al. (2011); Desai et al. (2012); Mohr et al. (2012), begins with initial image processing on single-exposure images and astrometry measurements from the software package SCAMP (Bertin 2006). The single-exposure images were then stacked to produce co-add images using the software package SWARP (Bertin et al. 2002). Basic object detection,

point-spread-function (PSF) modelling, star-galaxy classification[2] and photometry were done on the individual images as well as the co-add images using software packages SEXTRACTOR (Bertin & Arnouts 1996) and PSFEX (Bertin 2011). The full SVA1 Gold dataset consists of 254.4 deg^2 with $griz$-band coverage, and 223.6 deg^2 for Y band. The main science goal for this work is to reconstruct wide-field mass maps; as a result, we use the largest continuous region in the SV data: 139 deg^2 in the SPT-E field.

The SVA1 Gold Catalog is augmented by: a photometric redshift catalog, two galaxy shape catalogs, and an LRG catalog. These catalogs are described below.

3.1.1   Photometric redshift catalog

In this work we use the photometric redshift (photo-z) estimated with the Bayesian Photometric Redshifts (BPZ) code (Benítez 2000; Coe et al. 2006). The photo-z's are used to select the main foreground and background sample (see §3.2). The details and capabilities of BPZ on early DES data were already presented in Sánchez et al. (2014), where it showed good performance among template-based codes. The primary set of templates used contains the Coleman, Wu & Weedman (1980) templates, two starburst templates from Kinney et al. (1996) and two younger starburst simple stellar population templates from Bruzual & Charlot (2003), added to BPZ in Coe et al. (2006). We calibrate the Bayesian prior by fitting the empirical function $\Pi(z, t|m_0)$ proposed in Benítez (2000), using a spectroscopic sample matched to DES galaxies and weighted to mimic the photometric properties of the DES SV sample used in this work. As tested in Sánchez et al. (2014), the bias in the photo-z estimate is $\sim$0.02, with 68% scatter $\sigma_{68} \sim 0.1$ and the 3σ outlier fraction $\sim$2%. For this work, we use z_{mean}, the mean of the Probability Distribution Function (PDF) output from BPZ as a single-point estimate of the photo-z to separate our galaxies into the foreground and background samples. Other photo-z codes used in DES have been run on the same data. For this work we have also checked our main results in §5 using an independent Neural Network code (Skynet; Bonnett 2013; Graff & Feroz 2013). We found that BPZ and Skynet gives consistent results (within 1σ) in terms of the cross-correlation between the weak lensing mass maps and the foreground galaxy map.

3.1.2   Shape catalogs

Based on the SVA1 data, two shear catalogs were produced and tested extensively in Jarvis et al. (in preparation): the ngmix[3] (version 011) catalog and the im3shape[4] (version 9) catalog. The main results shown in our paper are based on the ngmix catalog, but we also cross-check with the im3shape catalog to confirm that the results are statistically consistent.

The PSF model for both methods are based on the single-exposure PSF models from PSFEx. PSFEx models the PSF as a linear combination of small images sampled on an ad hoc pixel

---

[2] We adopt the "MODEST_CLASS" classifier, which is a new classifier used for SVA1 Gold that has been developed empirically and tested on DES imaging of COSMOS fields with Hubble Space Telescope ACS imaging.
[3] The open source code can be downloaded at: https://github.com/esheldon/ngmix
[4] The open source code can be downloaded at: https://bitbucket.org/joezuntz/im3shape/

Table 1. Catalogs and cuts used to construct the foreground and background sample for this work, and the number of galaxies in each sample after all the cuts are applied. All catalogs are based on the DES SVA1 dataset.

	Background		Foreground main	Foreground LRG
Input catalog	ngmix011	im3shape	SVA1 Gold	Redmagic
Photometric redshift	0.6<z<1.2		0.1<z<0.5	0.2<z<0.5
Others	"conservative additive"		MAG_AUTO_I<22	constant density 10^{-3} $(h^{-1}Mpc)^{-3}$
Number of galaxies	1,111,487	1,013,317	1,106,189	28,033
Number density (arcmin^{-2})	2.22	2.03	2.21	0.056
Mean redshift	0.826	0.825	0.367	0.385

grid, with coefficients that are the terms of a second-order polynomial of pixel coordinates in each DECam CCD.

ngmix (Sheldon 2014) is a general tool for fitting models to astronomical images. For the galaxy model, ngmix supports various options including exponential disk and de Vaucouleurs' profile (de Vaucouleurs 1948), all of which are implemented approximately as a sum of Gaussians (Hogg & Lang 2013). Additionally, any number of Gaussians can be fit. These Gaussian fits can either be completely free or constrained to be co-centric and co-elliptical. For the DES SV galaxy images, we used the exponential disk model. For the PSF fitting, an Expectation Maximization (Dempster, Laird & Rubin 1977) approach is used to model the PSF as a sum of three free Gaussians. Shear estimation was carried out using by jointly fitting multiple images in r, i, z bands. The multi-band approach enabled a larger effective galaxy number density compared to the im3shape catalog, which is based on single-band images in the current version.

The im3shape (Zuntz et al. 2013) implementation in this work estimates shapes by jointly fitting a parameterized galaxy model to all of the different single-exposure r-band images, finding the maximum likelihood solution. Calibration for bias in the shear measurement associated with noise (Refregier et al. 2012; Kacprzak et al. 2012) is applied. An earlier version of this code (run on the co-add images instead of single-exposures) has been run on the SV cluster fields for cluster lensing studies (Melchior et al. 2015).

Details for both shape catalogs and the tests performed on these catalogs can be found in Jarvis et al. (in preparation). Both shear catalogs have been tested and shown to pass the requirements for SV cosmic shear measurement, which is much more stringent than what is required in this paper. As our analysis is insensitive to the overall multiplicative bias in the shear measurements, we adopt the "conservative additive" selection tested in that paper; this results in small additive systematic uncertainties, but possibly some moderate multiplicative systematic uncertainties. For ngmix, this cut removes galaxies with S/N<20 and very small galaxies (Gaussian sigma smaller than the pixel scale). For im3shape, it removes galaxies with S/N<15. In both cases, there were many other cuts applied to both catalogs to remove stars, spurious detections, poor measurements, and various other effects that significantly biased shear estimates for both catalogs. Further details are given in Jarvis et al. (in preparation).

3.1.3 The red-sequence Matched filter Galaxy Catalog (Redmagic)

We use the DES SV red-sequence Matched-filter Galaxy Catalog (Redmagic Rozo et al., in preparation) v6.3.3 in this paper as a sec-

ond foreground sample. The objects in this catalog are photometrically selected luminous red galaxies (LRGs). We use the terms Redmagic galaxies and LRG interchangeably. Specifically, Redmagic uses the Redmapper-calibrated model for the color of red-sequence galaxies as a function of magnitude and redshift (Rykoff et al. 2014). This model is used to find the best-fit photometric redshift for all galaxies irrespective of type, and the χ^2 goodness-of-fit of the model is computed. For each redshift slice, all galaxies fainter than some minimum luminosity threshold $L_{\min}$ are rejected. In addition, Redmagic applies a χ^2 cut $\chi^2 \leqslant \chi^2_{\max}$, where the cut $\chi^2_{\max}$ as a function of redshift is chosen to ensure that the resulting galaxy sample has a nearly constant space density $\bar{n}$. In this work, we set $\bar{n} = 10^{-3} h^3 \mathrm{Mpc}^{-3}$. We assume flat Λ CDM model with cosmological parameters $\Omega_\Lambda = 0.7$, $h = 100$ (varying these parameters does not change the results significantly). The luminosity cut is $L \geqslant 0.5 L_*(z)$, where the value of $L_*(z)$ at z=0.1 is set to match the Redmapper definition for SDSS, and the redshift evolution for $L_*(z)$ is that predicted using a simple passive evolution starburst model at $z = 3$. We use the Redmagic sample because of the exquisite photometric redshifts of the Redmagic galaxy catalog: Redmagic photometric redshifts are nearly unbiased, with a scatter $\sigma_z/(1+z) \approx 1.7\%$, and a $\approx 1.7\%$ 4σ redshift outlier rate. We refer the reader to Rozo et al. (in preparation) for further details of this catalog.

3.2 Foreground and background galaxy samples selection

As described in §1, the main goal of this paper is to construct a projected mass map at a given redshift via weak lensing and to show that the mass map corresponds to real structures, or mass, in the foreground line-of-sight. For that purpose, we define two galaxy samples in this study — the background "source" sample which is lensed by foreground mass, and the foreground "lens" sample that traces the foreground mass responsible for the lensing. We wish to construct a weak lensing mass map from the background sample according to §2.2 and compare it with the mass map generated from the foreground galaxy density map according to §2.3.

We choose to have the two samples separated at redshift ~ 0.55 in order to have a sufficient number of galaxies in both samples. Given that the photo-z training sample of our photo-z catalog does not extend to the same redshift and magnitude range as our data, we exclude objects with photo-z outside the range 0.1–1.2. The final foreground and background sample are separated by the photo-z cut of $0.1 < z < 0.5$ and $0.6 < z < 1.2$. Note that the Redmagic foreground galaxy sample has an additional redshift threshold $z > 0.2$.

The main quantity of interest for the background galaxy sample is the shear measured for each galaxy. Since the background
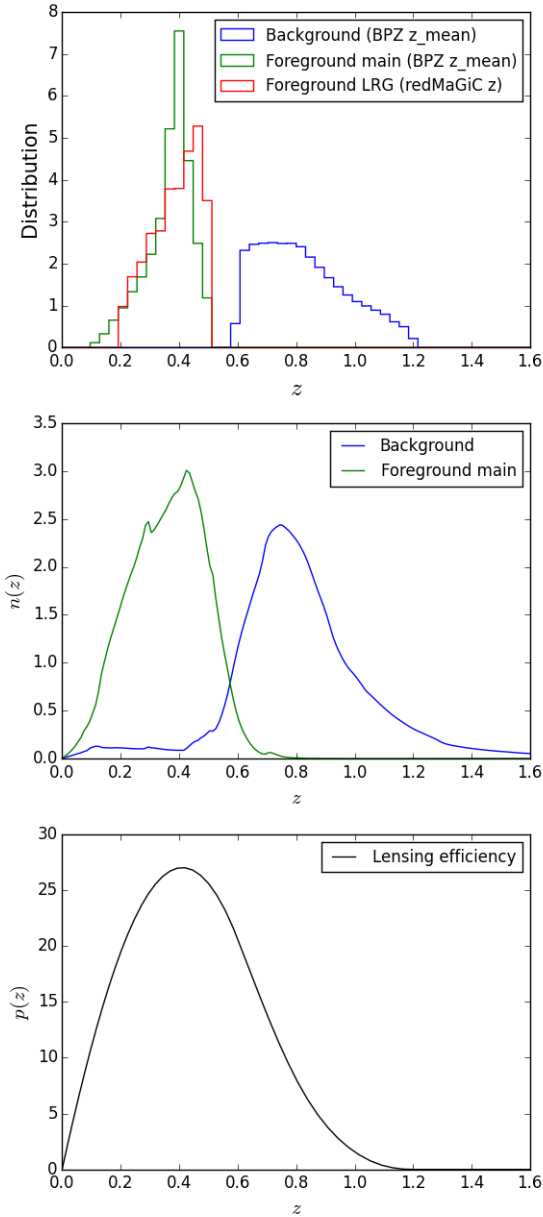
Figure 1. Distributions of the single-point photo-z estimates for the background and foreground samples used in this paper are shown in the top panel. The background and the foreground main sample uses the mean of the PDF from BPZ for single-point estimates, while the LRG redshift estimate comes independently from Redmagic (see §3.1.3). The second panel shows the corresponding $n(z)$ of the background and foreground main sample given by BPZ. These come from the sum of the PDF for all galaxies in the samples. The lensing efficiency (Equation 10) corresponding to the background sample is shown in the third panel.

sample only serves as a "backlight" for the foreground structure we are interested in, it need not be complete. Therefore the most important selection criteria for the background sample is to use galaxies with accurate shear measurements. Our source selection criteria are based on extensive tests of shear catalog as described in Jarvis et al. (in preparation). After applying the conservative selection of background galaxies and our background redshift cut we are left

with 1,111,487 galaxies (2.22/arcmin^2) for `ngmix` and 1,013,317 galaxies (2.03/arcmin^2) for `im3shape`.

The foreground sample in this work serves as the tracer of mass. Thus it is important to construct a magnitude-limited sample for which the number density is affected as little as possible by external factors. The main physical factors that contribute to variation in the galaxy number density are the spatial variation in depth and seeing. Both effects can introduce spatial variation in the foreground galaxy number density, which can be wrongly identified as foreground mass fluctuations. We test both effects in Appendix A. Two subsamples are used in this work as foreground samples: the "main" foreground sample and the LRG foreground sample. While the space density of LRGs is significantly lower than that of the main sample, they are better tracers of galaxy clusters and groups, so we use them to check our results. The main foreground sample includes all the galaxies with $i < 22$ and the LRG sample includes the LRGs in the Redmagic LRG catalog with $i < 22$. This magnitude selection is based on tests described in Appendix A1 to ensure that our sample is shallower than the limiting magnitude for all regions of sky under study. The final main foreground sample contains 1,106,189 galaxies (2.21/arcmin^2), while the LRG sample contains 28,033 galaxies (0.05/arcmin^2). Table 1 summarizes all the selection criteria and cuts applied on the three main samples used in this work.

Figure 1 shows the distributions of the single-point photo-z estimates (z_{mean}) for the final foreground and background samples (top panel), the $n(z)$ (from the BPZ code) for the background and main foreground sample (second panel), and the lensing efficiency corresponding to the background sample (bottom panel). Note that the background galaxy number density is lower than expected for other weak lensing applications as we have made stringent redshift cuts to avoid overlap between the foreground and background samples.

3.3 Mock catalogs from simulations

To validate the mass reconstruction procedure we use a set of simulated galaxy catalogs "Aardvark v1.0c" developed for the DES collaboration (Busha et al. 2013). The full catalog covers 1/4 of the sky and is complete to the final expected DES depth.

The heart of the galaxy catalog generation is the algorithm Adding Density Determined Galaxies to Lightcone Simulations (ADDGALS; Busha et al. 2013), which aims at generating a galaxy catalog that matches the luminosities, colors, and clustering properties of the observed data. The simulated galaxy catalog is based on three flat ΛCDM dark matter-only N-body simulations, one each of a 1050 Mpc/h, 2600 Mpc/h and 4000 Mpc/h boxes with 1400^3, 2048^3 and 2048^3 particles respectively. These boxes were run with `LGadget-2` (Springel 2005) with `2LPTic` initial conditions from Crocce, Pueblas & Scoccimarro (2006) and `CAMB` (Lewis & Bridle 2002). From an input luminosity function, galaxies are drawn and then assigned to a position in the dark matter simulation volume according to a statistical prescription of the relation between the galaxy's magnitude, redshift and local dark matter density. The prescription is derived from a high-resolution simulation using SubHalo Abundance Matching techniques (Conroy, Wechsler & Kravtsov 2006; Reddick et al. 2013; Busha et al. 2013). Next, photometric properties are assigned to each galaxy, where the magnitude-color-redshift distribution is designed to reproduce the observed distribution of SDSS DR8 and DEEP2 data. The size distribution of the galaxies is magnitude-dependent and modelled from a set of deep ($i \sim 26$) SuprimeCam i-band images, which were

taken at with seeing conditions of 0.6". Finally, the weak lensing parameters (κ and γ) in the simulations are based on the ray-tracing algorithm Curved-sky grAvitational Lensing for Cosmological Light conE simulatioNS (CALCLENS; Becker 2013). The ray-tracing resolution is accurate to $\simeq 6.4$ arcseconds, sufficient for the usage in this work.

Aside from the intrinsic uncertainties in the modelling in the mock galaxy catalog (related to the input parameters and uncertainty in the galaxy-halo connection), there are also many real-world effects that are not included in these simulations, including as depth variation, seeing variation and shear measurement uncertainties. As a result, we use the simulations primarily as a tool to understand the impact of various effects on the expected signal, and a sanity check to confirm that our measurement method is producing reasonable results.

4 RESULTS: MASS MAPS AND GALAXY CLUSTERS

In Figure 2 we show our final convergence maps generated using the data described in §3.1 and the methods described in §2.2 and §2.3. For the purpose of visualization we present maps for 20 arcmin Gaussian smoothing. In the top left panel we show the E-mode convergence map generated from shear. The top right panel shows the weighted foreground galaxy map from the main sample, $\kappa_{g,main}$ map. In both of these panels, red areas correspond to over-densities and blue areas correspond to under densities. The bottom left and bottom right panels show the product of the κ_E (left) and κ_B (right) maps with the $\kappa_{g,main}$. Visually we see that there are more positive (correlated) areas for the κ_E map compared to the κ_B map, indicating clear detection of the weak lensing signal in these maps. Note that these positive regions could be either mass over-densities or under-densities. In §5, we present a quantitative analysis of this correlation.

4.1 Noise estimates for the mass maps

To estimate the significance of the structures in the mass maps, it is important to understand the noise properties of these maps. Uncertainties in the lensing convergence map include contributions from both shape noise and measurement uncertainties, which is affected by the number density of galaxies across the field and the shear measurement method.

We estimate the uncertainties on each pixel by randomising the shear measurements on each galaxy. A thousand random background galaxy catalogs were generated by shuffling the shear values between all the galaxies. We then construct κ_E and κ_B maps from these randomized catalogs in the same way as in Figure 2. The RMS map for these 1000 random samples is used as the noise map. Dividing the signal map (Figure 2) by the noise map gives an estimate for the S/N of the different structures in the maps, as shown in Figure 3. These values are consistent with those predicted via Equation 13 and simulations described in §5.2. The bottom panels of Figure 3 show the distribution of the S/N values for both E and B-mode maps for data as well as simulations. We find that the B-mode distribution is consistent with a Gaussian distribution and the E-mode gives more extreme values.

4.2 Correlation with known structures

In this section we compare our mass map with optically identified clusters using Redmapper v6.3.3 (Rykoff et al. in preparation) from

DES data. We compare optically identified groups and clusters of galaxies in our data based on Redmapper with the reconstructed mass map. We overlay in Figure 4 Redmapper clusters and groups on the mass map as black circles. The size of these circles corresponds to the optical richness of these structures. Also, only objects with optical richness λ greater than 20 and redshift between 0.1 and 0.5 are shown in the figure. According to Rykoff et al. (2012) and Saro et al. (in preparation), this corresponds to cluster masses larger than a few times $10^{14}\,M_\odot$. It is evident from this figure that the structures in the weak lensing mass map have significant correlation with the distribution of optically identified Redmapper clusters.

From the mass and galaxy maps in Figure 2 and Figure 4 we identified large peaks at the positions (RA, DEC) = (71.0, -45.0), (70.0, -47.8), (69.8, -54.5) and (69.1, -57.3), and large voids at (RA, DEC) = (65.7, -49.0), (74.8, -54.8), (75.7, -58.0), (82.8, -59.5). Analyzing the redshift distribution of the foreground structure at these locations shows that the peaks indeed correspond to supercluster like structures that are typically localized in the redshift range $0.3 - 0.4$, though in at least one case there is evidence for multiple structures at different redshifts. The tight photo-z accuracy of the Redmapper clusters ($\sigma_z \approx 0.01(1+z)$) gives us some confidence in the identification of real 3D structures. The transverse spatial extent of the superclusters is typically greater than 10 Mpc. We believe this approach provides a powerful tool for identifying superstructures in the Universe which would otherwise be hard to spot. The size and mass of the superclusters are of interest for cosmology as they represent the most massive end of the matter distribution. We defer more detailed studies of the superclusters and voids to follow up work.

5 RESULTS: MASS MAPS AND CORRELATION WITH GALAXY DISTRIBUTION

In this section we quantitatively analyze the extent to which mass follows galaxy density in the data. To do this, we cross-correlate the weak lensing mass map with the weighted foreground galaxy density map. The correlation is quantified via the Pearson cross-correlation coefficient as described in §5.1. We cross check the results using simulations in §5.2.

5.1 Quantifying the galaxy-mass correlation

We smooth both the convergence maps generated from weak lensing and from the foreground galaxy density with a Gaussian filter. These smoothed maps are used to estimate the correlation between the foreground structure and the weak lensing convergence maps. We calculate the correlation as a function of the smoothing scale (*i.e.* the size of the Gaussian filter). The correlation is quantified via the Pearson correlation coefficient defined as

$$\rho_{\kappa_E \kappa_g} = \frac{\langle \kappa_E \kappa_g \rangle}{\sigma_{\kappa_E} \sigma_{\kappa_g}}, \tag{16}$$

where $\langle \kappa_E \kappa_g \rangle$ is the covariance between κ_E and κ_g; σ_{κ_E} and σ_{κ_g} are the standard deviation of the κ_E map, and the κ_g map from either the foreground main galaxy sample or the foreground LRG sample. In this calculation, pixels in the masked region are not used. We also remove pixels within 10 arcmin of the boundaries to avoid significant artefacts from the smoothing.

Figure 5 shows the Pearson correlation coefficient as function of smoothing scales from 2 to 40 arcmin. We find that there
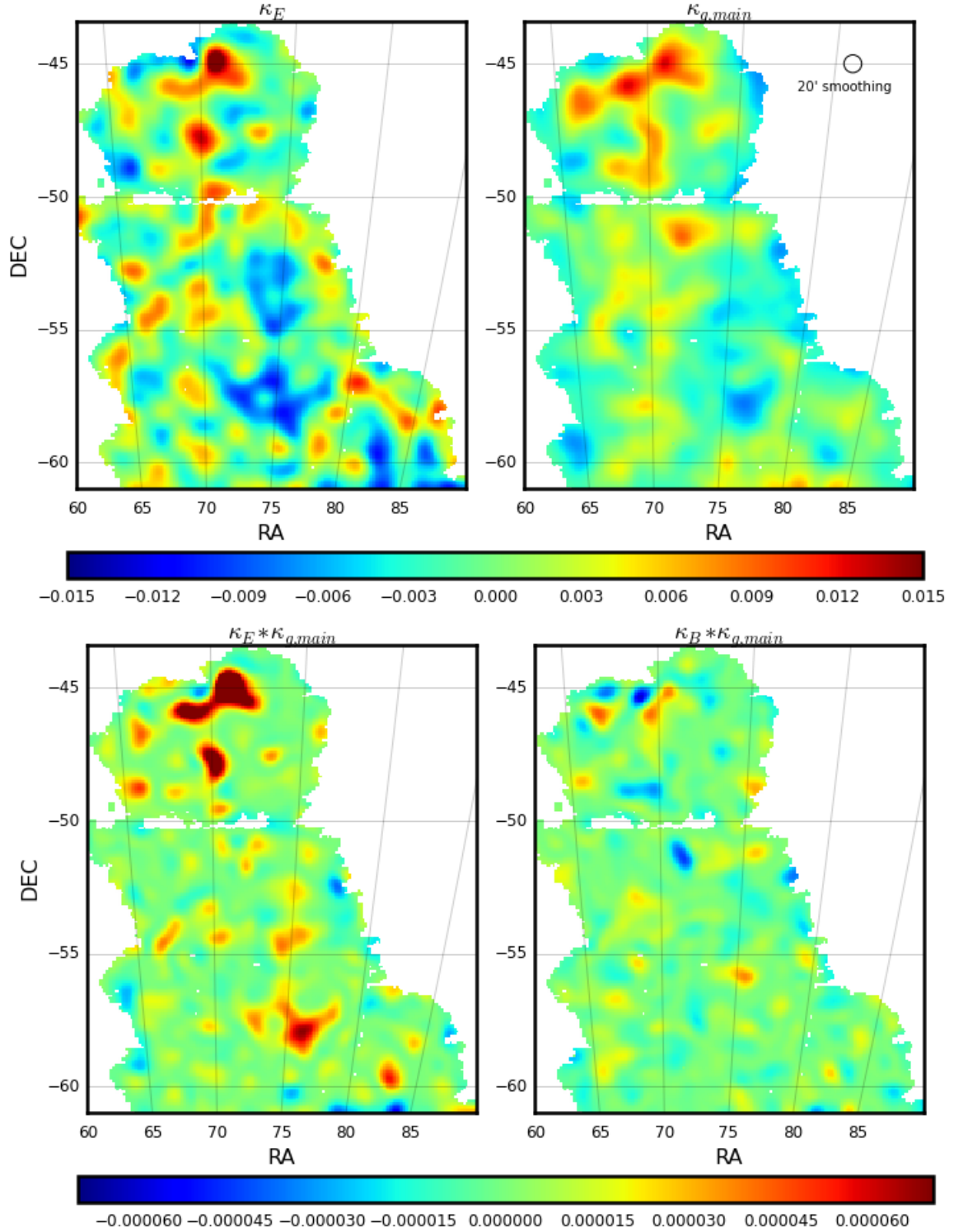
Figure 2. The upper left panel shows the E-modes of the weak lensing convergence map. The upper right shows the weighted foreground galaxy map from the main sample, or $\kappa_{g,main}$. The lower two panels show the product maps of the E-mode (left) and B-mode (right) convergence map with the $\kappa_{g,main}$ map. All maps are generated with a 5 arcmin pixel scale and 20 arcmin Gaussian smoothing. Red areas corresponds to overdensities and blue areas to underdensities in the upper panels. White regions correspond to the survey mask. The scale of the Gaussian smoothing kernel is indicated by the circle on the upper right corner, with a radius of 20 arcmin (the equivalent radius of a top-hat kernel is larger by a factor of $\sqrt{2}$).
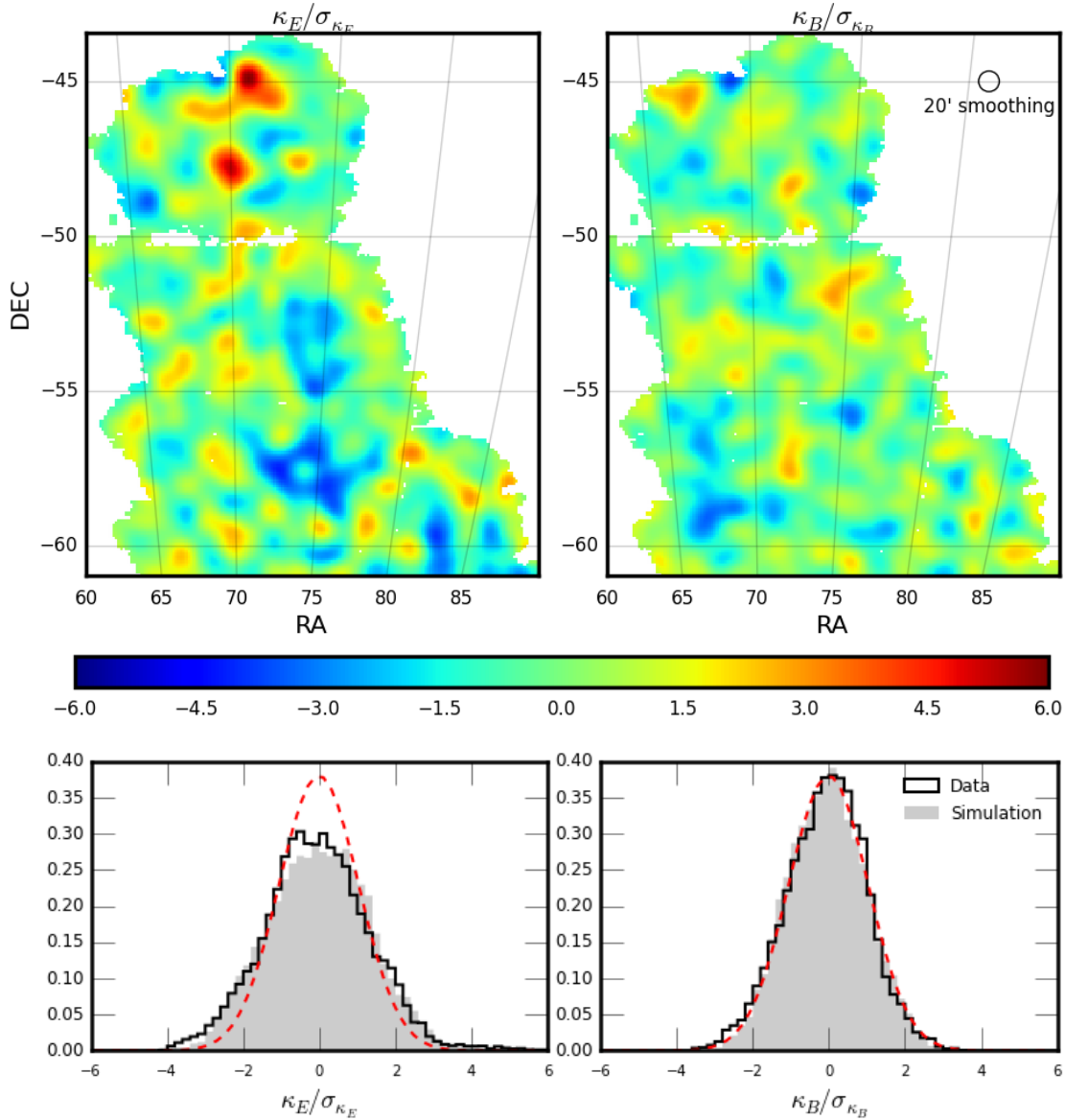
Figure 3. The top panel shows the S/N map for the mass map in Figure 2 estimated via randomized errors described in §4.1. Note that due to the Gaussian smoothing kernel, there is some mixing of scales which leads to higher contrasts in the cores of over and under-dense regions compared to top-hat smoothing. The bottom panel shows the normalized S/N distributions for both maps, overlaid by those measured from simulations described in §5.2. The red dashed lines in both bottom panels show a Gaussian fit to the B-mode S/N.

is significant correlation between the weak lensing E-mode convergence and convergence from different foreground samples, with increasing correlation towards large smoothing scale. This trend is expected for noise-dominated maps, because the larger smoothing scales reduce the noise fluctuations in the map significantly. A similar trend is found when using the LRGs as foreground instead of the general magnitude-limited galaxy sample. The lower Pearson correlation between the mass map and LRG sample is because of the larger shot noise due to the lower number density compared to the magnitude-limited foreground sample. The error bar on the correlation coefficient is estimated based on jackknife resampling. We divide the observed sky into jackknife regions of size 10 deg^2 and recalculate the Pearson correlation coefficients, excluding one

of the 10 deg^2 regions each time. We found that the estimated uncertainties do not depend significantly on the exact value of patch size. We estimate the correlation coefficient after removing one of those patches from the sample to get jackknife realizations of the cross-correlation coefficient ρ_j. Finally, the variance is estimated as

$$\Delta\rho = \frac{N-1}{N}\sum_j (\rho_j - \bar{\rho})^2, \qquad (17)$$

where j runs over all the N jackknife realizations and $\bar{\rho}$ is the average correlation coefficients of all patches.

We find that the Pearson correlation coefficient between κ_g from the main foreground galaxy sample (LRG sample) and weak
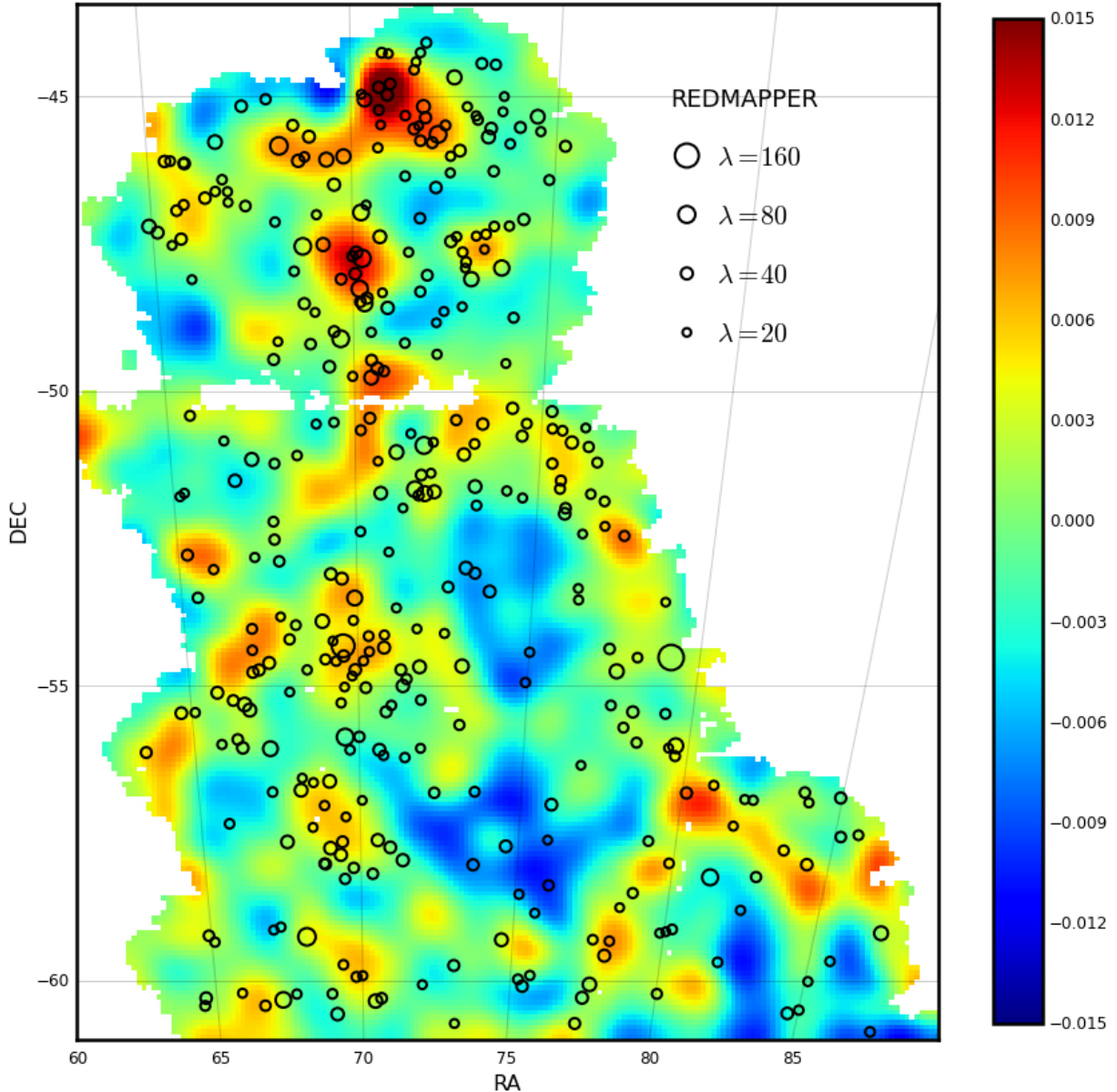
Figure 4. The DES SV mass map along with foreground galaxy clusters detected using the Redmapper algorithm. The clusters are overlaid as black circles with the size of the circles indicating the richness of the cluster. Only clusters with richness greater than 20 and redshift between 0.1 and 0.5 are shown in the figure. The upper right corner shows the correspondence of the optical richness to the size of the circle in the plot. It can be seen that there is significant correlation between the mass map and the distribution of galaxy clusters. Several superclusters and voids can be identified in the joint map.

lensing E-mode convergence is 0.39 ± 0.06 (0.36 ± 0.05) at 10 arcmin smoothing and 0.52 ± 0.08 (0.46 ± 0.07) at 20 arcmin smoothing. This corresponds to a $\sim 6.8\sigma$ (7.5σ) significance at 10 arcmin smoothing and $\sim 6.8\sigma$ (6.4σ) at 20 arcmin smoothing. As a zeroth-order test of systematics we also estimated the correlation between the B-mode weak lensing convergence and the κ_g maps. We find that the correlation between κ_B and the main foreground sample is consistent with zero at all smoothing scales. Similarly, the correlation between E and B modes of κ is consistent with zero. For comparison, we show the same plot calculated for the `im3shape` catalog in Figure 6. We find very similar results, with slightly larger correlation between κ_E and κ_B at the 1σ level.

5.2 Comparison with mock catalogs

At this point, it is important to verify whether our measurements in the data are consistent with what is expected. We investigate this using the simulated catalogs described in §3.3. As the simulations lack several realistic systematic effects in the data, these tests mainly serve as a guidance for us to understand: (1) the origin of the B-mode in the κ maps, (2) the approximate expected level of $\rho_{\kappa\kappa_g}$ under pixelization and smoothing, (3) the effect on $\rho_{\kappa\kappa_g}$ from photo-z uncertainties and cosmic variance, and (4) the effect on the maps and $\rho_{\kappa\kappa_g}$ from the survey mask.

We construct a sample similar to the SV data. The same redshift, magnitude, and number density cuts in Table 1 are applied to the simulations to form a foreground and a background sample. We
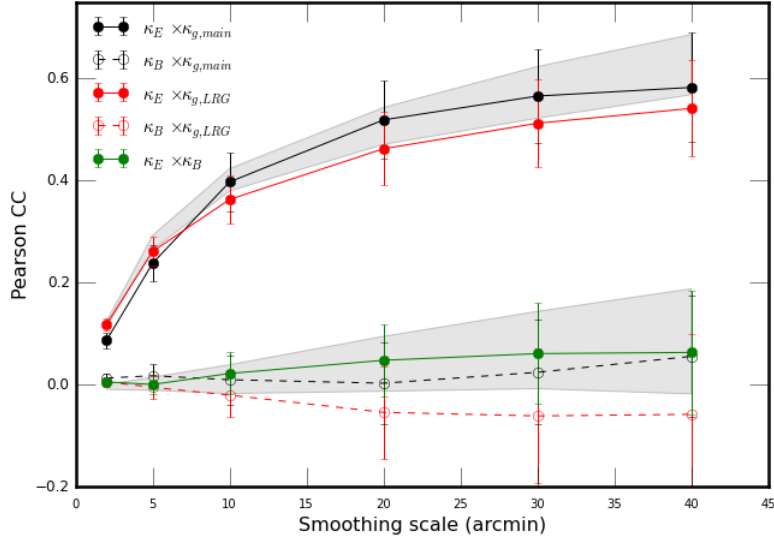
Figure 5. This figure shows the Pearson correlation coefficient between foreground galaxies and convergence maps as a function of smoothing scale. The solid and open symbols show the E and B-mode correlation coefficients respectively. The black circles are for the main foreground sample and the red circles for foreground LRGs. The grey shaded regions show the 1σ bounds for E and B mode correlations from simulations for the main foreground sample with the same pixelization and smoothing (see §5.2 for details). We do not show the same simulation results for the LRG sample. The detection significance for the correlation is in the range $\sim 5-7\sigma$ at different smoothing scales. The green points show the correlation between E and B-modes of the mass map. The various B-mode correlations are consistent with zero. Uncertainties on all measurements are estimated based on jackknife resampling.
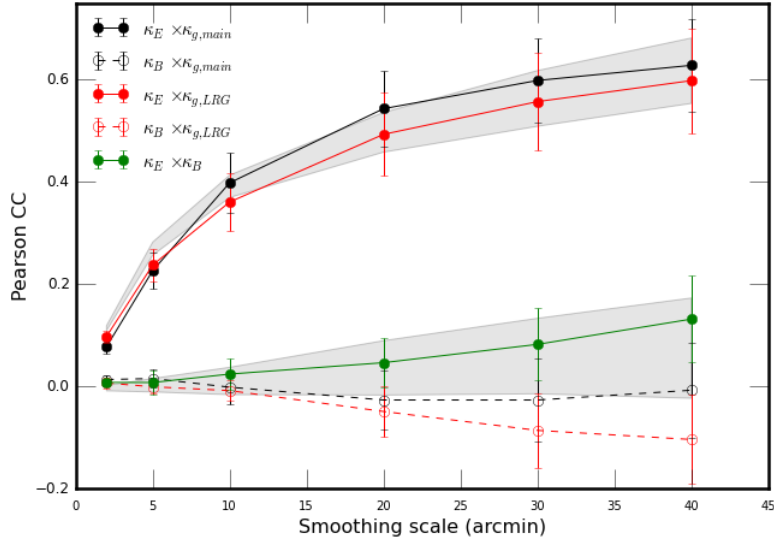
Figure 6. Same as Figure 5 but using the `im3shape` galaxy catalog.

choose to simulate the main foreground sample as the LRG foreground sample selection in the simulations is less controllable. For the background sample, we add a random Gaussian of RMS 0.29 per component to the true shear in the simulations to generate a model for the ellipticities that matches the data. We then create a κ_g map from the main foreground sample and a κ map from the background sample the same way as is done in the data. The cross-correlation coefficient $\rho_{\kappa\kappa_g}$ is calculated from these simulated maps as in §5. We consider the same range of smoothing scales for the maps when calculating $\rho_{\kappa\kappa_g}$ as that in Figure 6.

The simulations provide us a controlled way of separating the different sources of effects. We construct the maps in the following

steps, in order of increasing similarities to data: (1) pixelating and smoothing the true κ values; (2) constructing the κ values from the true γ values; (3) construct the κ values from the galaxy ellipticities; (4) repeat (3) using a photo-z model for the foreground and the background instead of the true redshift; (5) repeat (4) for different regions on the sky; (6) repeat (5) with the SV survey mask.

The difference between (1) and (2) measures the quality of the KS reconstruction method. The difference between (2) and (3) shows the effect of shape noise and measurement noise. Steps (4), (5) and (6) then show the effect of photo-z uncertainties, cosmic variance and masking. Note that we estimate the effect of sample variance by generating maps for 4 different regions on the sky. Also
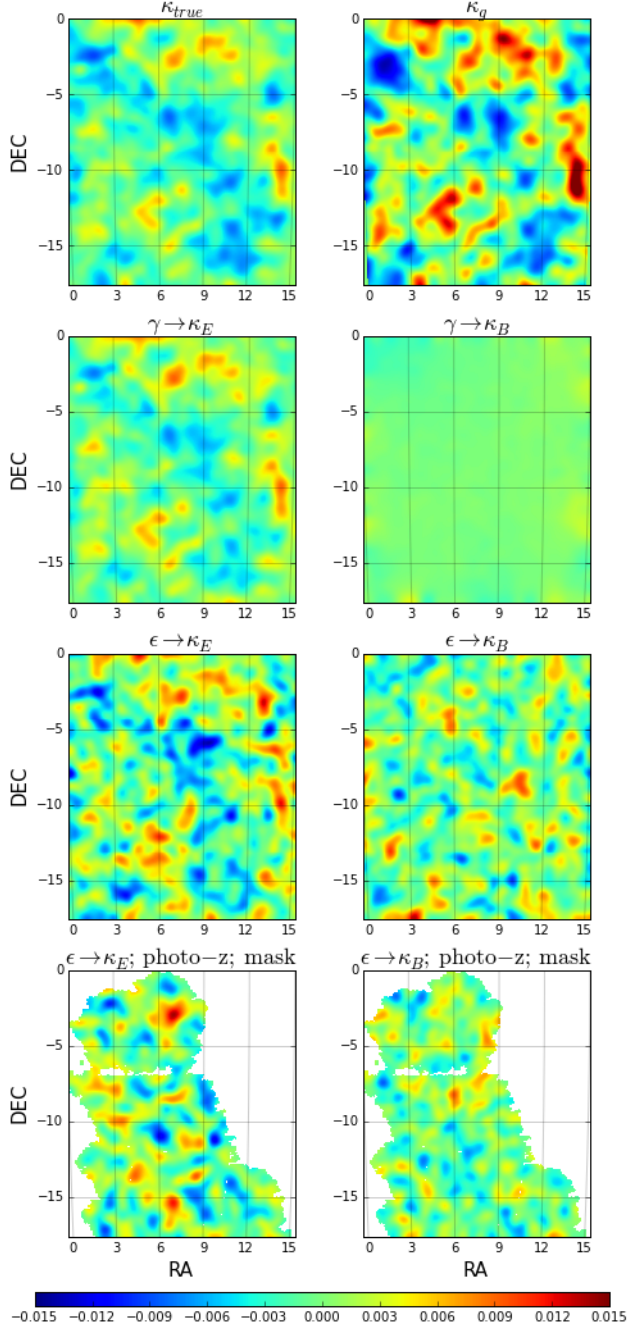
Figure 7. Maps from simulations that are designed to mimic the data in our analysis. The simulations are generated for a field of size $15 \times 17.6 \deg^2$ with similar redshift and magnitude cuts for the foreground and the background sample as the data. The true κ and κ_g maps are shown in the first row, where κ_g is modelled for the main foreground sample. The reconstructed κ_E and κ_B maps from the true γ are shown in the first two panels of the second row, followed by the κ_E and κ_B maps reconstructed from the ellipticity (ε) values. The last row first shows the κ_E and κ_B constructed from ε with photo-z uncertainties, then the same maps with an SV survey mask applied. The last two panels on the bottom most closely match the data.
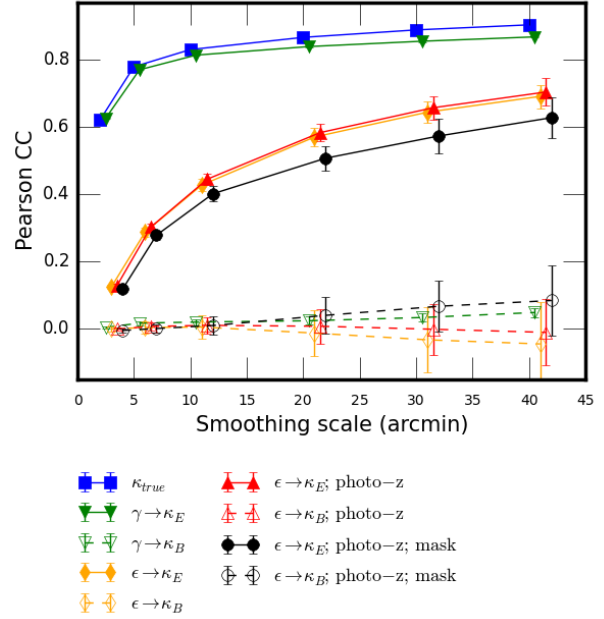
Figure 8. Pearson correlation coefficient $\rho_{X\kappa_g}$ between the different simulated maps shown in Figure 7 as a function of smoothing scale. X represents the different κ maps as listed in the legend. This plot is the simulation version of Figure 5, where one can see how the measured values in the data could have been degraded due to various effects. The qualitative trend of the correlation coefficients as a function of smoothing scale is consistent with that observed in data. When reconstructing κ_E from the true γ small errors are introduced due to the nonlocal reconstruction, lowering the correlation coefficient by a few percent. Adding shape noise to the shear measurement lowers the signal significantly, with the level of degradation dependent on the smoothing scale. Adding photo-z uncertainties changes the signal by a few percent. Finally, placing an SV-like survey mask changes the signal by $\sim 10\%$. The black curve with its error bars corresponds to the shaded region in Figure 5.

for the steps (4)-(6) above, we generate each of the maps with 20 different realisations of the shape noise.

5.2.1 Maps from simulations

Figure 7 shows the various maps generated from one particular patch of the simulations in this procedure for 5 arcmin pixels and 20 arcmin smoothing scales (consistent with that in Figure 2). The amplitude of κ_E and κ_B both become larger than in the true maps when shape noise is added, and the resulting κ_E map has only slightly higher contrast than the κ_B map. When photo-z uncertainties are included, we see that the peaks and voids in the κ_E maps visibly move around. Applying the mask mainly changes the morphology of the structures in the maps around the edges. Comparing the last κ_E panel in Figure 7 and Figure 2, we see that the amplitude and qualitative scales of the variation in the κ_E maps are similar. On the other hand, if we compare the κ_g maps in the simulations with the κ_g maps in Figure 2, we find some qualitative differences between the simulations and the data. The simulation contains more small scale structure and low-κ_g regions compared to the data. We do not investigate this issue further here, as the level of agreement in the simulations and the data is sufficient for our purpose.

5.2.2 Correlation coefficients from simulations

Figure 8 shows the mean Pearson correlation coefficient between the different maps as a function of smoothing scales for the 80 sets of simulated maps (4 different areas in the sky and 20 realisations of shape noise each). The error bars indicate the RMS spread of these 80 simulations.

We find that $\rho_{\kappa_{true}\kappa_g}$ is 10-20% below 1, which is the case for perfect correlation. Several factors contribute to this. First, the foreground galaxy sample only includes a finite redshift range, and not all galaxies that contribute to the κ_{true} map. Second, the presence of a redshift-dependent galaxy bias adds further complication to the correlation coefficient. The effect of converting from the true shear γ to convergence lowers the correlation coefficient by about 3%. This is a measure of the error in the KS conversion under finite area and resolution of the shear fields. The main degradation of the signal comes when shape noise and measurement noise is included. Photo-z uncertainties in both the foreground and the background sample changes the correlation coefficient slightly. Finally, the survey mask lowers the signal by $\sim 10\%$.

The final correlation coefficient after considering all the effects discussed above is shown by the black curve in Figure 8 and overplotted as the shaded region in Figure 5. We find that the dependence of $\rho_{\kappa\kappa_g}$ on the smoothing scale in the simulation is qualitatively and quantitatively very similar to that seen in Figure 5.

6 SYSTEMATIC EFFECTS

In §4.1 we evaluated the statistical uncertainties on the mass map and the correlation between the mass map and the foreground galaxy density maps. In this section we examine the possible systematic uncertainties in our measurement. We focus on the cross correlation between our weak lensing mass map κ_E and the main foreground density map $\kappa_{g,main}$. To simplify the notation, we omit the "main" in the subscript and use κ_g to represent the main foreground map in this section.

We investigate the potential contamination from systematic effects on the cross-correlation coefficient $\rho_{\kappa_E\kappa_g}$. That is, we consider the situation where part of the correlation between the mass map and the κ_g map is not cosmological, but rather caused by other physical systematic effects that are correlated with both maps simultaneously. We examine these systematic uncertainties in our measurement by looking at the spatial correlation of various quantities with the κ_E map and the κ_g map.

As discussed in Appendix A, there are several factors that can contaminate the δ_g maps. For example, depth and PSF variations in the observed field can introduce artificial clustering in the foreground galaxy density map. Although we use magnitude and redshift cuts according to the tests in Appendix A, one can expect some level of residual effects on the κ_g maps. The κ_E map is constructed from shear catalogs of the background sample, thus systematics in the shear measurement will propagate into the κ_E map. In Jarvis et al. (in preparation), extensive tests of systematics have been carried out on the shear catalog. Therefore here we focus on the systematics that are specifically relevant for mass mapping and the correlation coefficient Eqn. 16.

We identify several possible sources of systematics for the background and foreground sample as listed in Table 2. We generate maps of these quantities that are pixelated and smoothed on the same scale as the κ_E and κ_g maps. We then evaluate the contribution of these effects to the correlation coefficient (Eqn. 16) based

Table 2. Quantities examined in our systematics tests.

Map name	description
kE (signal)	κ_E from γ_1, γ_2 for background sample
kg (signal)	κ_g from main foreground sample
kB	κ_B from γ_1, γ_2 for background sample
ns	star number per pixel
ng_b	galaxy number per pixel for background sample
snr	signal-to-noise of galaxies in im3shape
mask	fraction of area masked in galaxy postage stamp
g1	average γ_1 for background sample
g2	average γ_2 for background sample
psf_e1	average PSF ellipticity
psf_e2	average PSF ellipticity
psf_T	average PSF size
psf_kE	κ_E generated from average PSF ellipticity
psf_kB	κ_B generated from average PSF ellipticity
zp_b	mean photo-z for background sample
zp_f	mean photo-z for foreground sample
ebv	mean extinction
skysigma	RMS sky brightness in ADU
sky	mean sky brightness in ADU
maglim	mean limiting i-band AB magnitude
exptime	mean exposure time in seconds
airmass	mean airmass

on the following simple diagnostic quantity:

$$\hat{\rho}_{\kappa_E\kappa_g;\Theta} = \frac{\hat{\rho}_{\kappa_E\Theta}\hat{\rho}_{\kappa_g\Theta}}{\hat{\rho}_{\Theta\Theta}} \quad (18)$$

with $\hat{\rho}_{XY}$ being the cross-correlation function, which is effectively the unnormalized Pearson correlation coefficient between X and Y, or

$$\hat{\rho}_{XY} = \langle XY \rangle. \quad (19)$$

Equation 18 measures the contribution from some systematics field Θ to $\hat{\rho}_{\kappa_E\kappa_g}$. We calculate $\hat{\rho}_{\kappa_E\kappa_g;\Theta}$ with Θ being any of the 20 quantities in Table 2 (excluding the signal). Figure 9 shows the normalized cross-correlation coefficient $\hat{\rho}_{\kappa_E\kappa_g;\Theta}/\hat{\rho}_{\kappa_E\kappa_g}$ values for all the quantities considered for 10 and 20 arcmin smoothing, with the red dashed line at 5%. The error bars are estimated by jackknife resampling similar to that described in §5.1, and the two panels show the results for ngmix and im3shape respectively. The normalized cross-correlation coefficient is a measure of the fractional contamination in the Pearson coefficient (Equation 16) from each of the systematics maps Θ.

We find that for ngmix all quantities show contributions to the systematic uncertainties at 10 arcmin smoothing to be at the level of 5% or lower, while the systematics increase to up to 15% when smoothing at the 20 arcmin scale (though with large error bars on the systematics estimation). For im3shape, most of the values stay below 5% for both smoothing scales. The largest contribution in both cases come from the variation in the PSF properties (psf_e1, psf_e2, psf_kB). Since all these PSF quantities are correlated with each other, and many other parameters (g1, g2, snr, maglim) are correlated with the PSF properties, we do not expect the total systematics contamination to be a direct sum of all these parameters. Instead, we discuss in Appendix B how one can isolate the independent contributions of the systematics via a Principal Component Analysis approach and correct for them. We find that the correction changes the final Pearson correlation coefficient by 3.5% relative to the original $\rho_{\kappa_E\kappa_g}$ measured in §5.

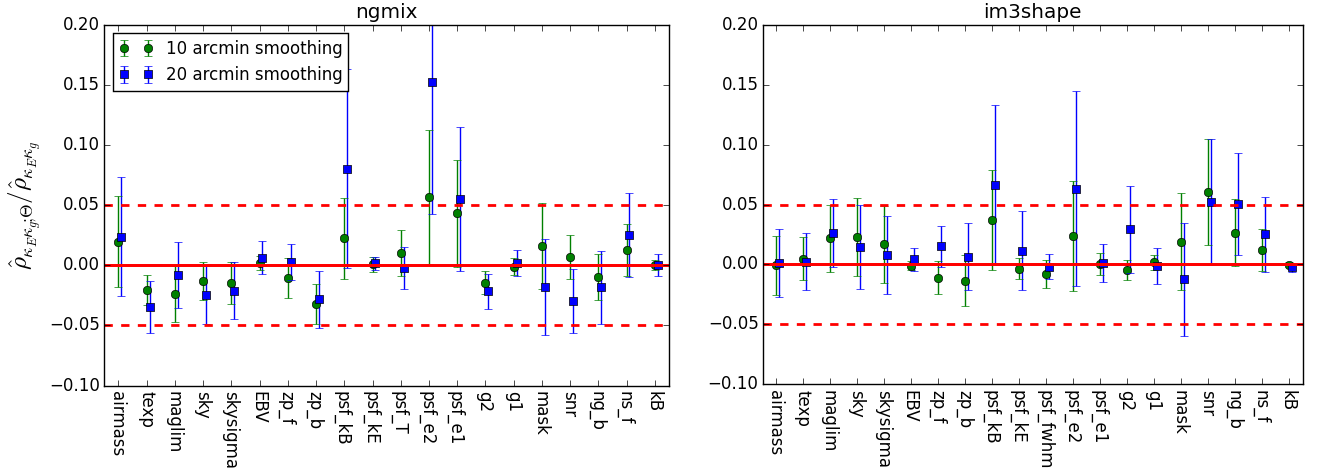Finally, to check the level of systematic contamination in our

Figure 9. The normalised cross-correlation coefficient $\hat{\rho}_{\kappa_E \kappa_g;\Theta}$ is shown for 20 different systematic uncertainty parameters. The systematics parameters, represented by Θ, are listed in Table 2 and shown for two smoothing scales. The $\hat{\rho}_{\kappa_E \kappa_g;\Theta}$ values are normalized by $\hat{\rho}_{\kappa_E \kappa_g}$ to show the relative magnitude of the systematic and the signal. The red dashed line indicates where the systematic is 5% of $\hat{\rho}_{\kappa_E \kappa_g}$. The error bars are estimated from resampling the foreground and background galaxy sample in patches of size 10 deg^2. The left panel is calculated for `ngmix` while the right panel is for `im3shape`.
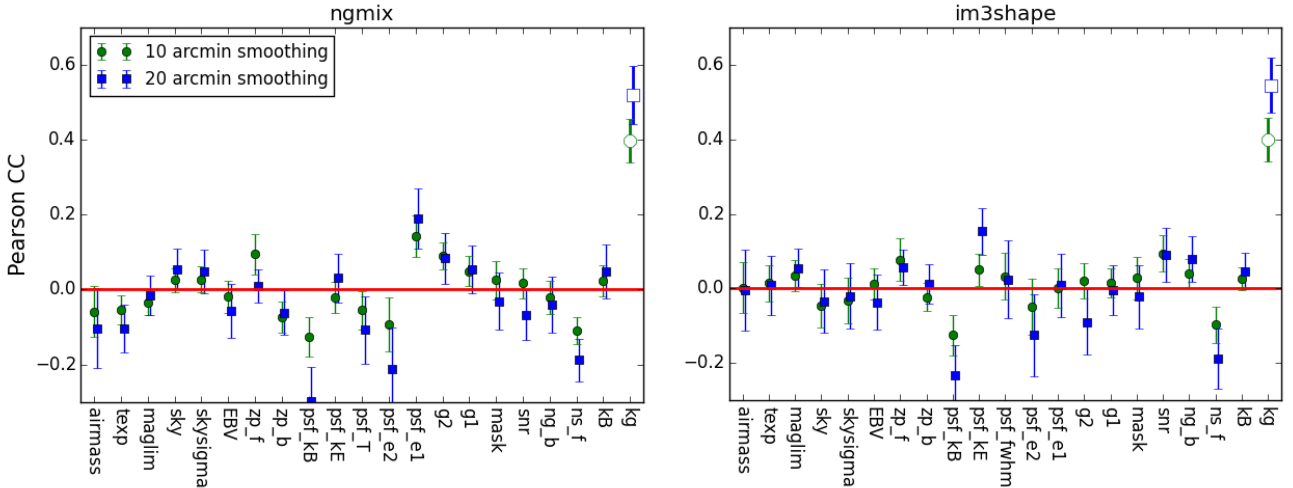
Figure 10. Pearson correlation coefficient $\rho_{\kappa_E \Theta}$ where Θ represents the quantities listed in Table 2. We show the statistics for two smoothing scales and for both `ngmix` (left) and `im3shape` (right). The right-most points in both panel correspond to the detection signal in Figure 5 and Figure 6. The error bars are estimated from resampling the foreground and background galaxy sample in patches of size 10 deg^2. Note that this is a different statistic from that in Figure 9, thus the y-axis values are not directly comparable.

κ_E map itself, we also calculate the Pearson correlation coefficient (Eqn. 16) between the various maps in Table 2 and our κ_E map. Note that this contamination may or may not be pronounced in Figure 9 since the statistics plotted there also take into account the correlation of κ_g with the various quantities. This test is independent of the foreground map, therefore is important for applications of the κ_E map that do not also use the foreground maps. Figure 10 shows the resulting 21 Pearson correlation coefficients. We find that the signal shown in the right-most points in the plot ($\rho_{\kappa_E \kappa_g}$) is larger than all other correlations by at least a factor of $\sim$3.

We also note that in both of these tests, the area of the map is not big enough to ignore the fact that some of these correlations can be intrinsically non-zero, even if there were no systematics contamination in the maps.

7 CONCLUSIONS

Weak lensing mass maps, or convergence maps, enable a number of cosmological studies: cross-correlations with galaxies, clusters and filaments, and with Sunyaev-Zel'dovich (SZ) or lensing maps from the cosmic microwave background (CMB). In addition, 2-point correlation functions of the convergence field provide a useful and simple check on the measurements made directly with the shear, while higher order correlations are easier to measure and interpret than those of the two-component shear field.

In this work, we present a weak lensing mass map based on galaxy shape measurements in the 139 deg^2 SPT-E field from the Dark Energy Survey Science Verification data. We have cross-correlated the mass map with maps of galaxy and cluster samples in the same dataset.

We constructed mass maps from the foreground Redmagic LRG and general magnitude-limited galaxy samples under the assumption that mass traces light. We find that the E-mode of the convergence map correlates with the galaxy based maps with high statistical significance. We repeated this analysis at various levels of smoothing scales and compared the results to measurements from mock catalogs that reproduce the galaxy distribution and lensing shape noise properties of the data. The Pearson cross-correlation coefficient is 0.39 ± 0.06 (0.36 ± 0.05) at 10 arcmin smoothing and 0.52 ± 0.08 (0.46 ± 0.07) at 20 arcmin smoothing for the main (LRG) foreground sample. This corresponds to a $\sim 6.8\sigma$ (7.5σ) significance at 10 arcmin smoothing and $\sim 6.8\sigma$ (6.4σ) at 20 arcmin smoothing. We get comparable values from the mock catalogs, indicating that statistical uncertainties, not systematics, dominate the noise in the data. The B-mode of the mass map is consistent with noise and its correlations with the foreground maps are consistent with zero at the 1σ level.

To examine potential systematic uncertainties in the convergence map we identified 20 possible systematic tracers such as seeing, depth, PSF ellipticity and photo-z uncertainties. We show that the systematics effects are consistent with zero at the 1 or 2σ level. In Appendix B, we present a simple scheme for the estimation of systematic uncertainties using Principal Component Analysis. We discuss how these contributions can be subtracted from the mass maps if they are found to be significant.

The results from this work open several new directions of study. Potential areas include the study of the relative distribution of hot gas with respect to the total mass based on X-ray or SZ observations, estimation of galaxy bias, constraining cosmology using peak statistics, and finding filaments in the cosmic web. The tools that we have developed in this paper are useful both for identifying potential systematic errors and for cosmological applications. The observing seasons for the first two years of DES are now complete (Diehl et al. 2014) and contain an area well over ten times that of the SV data, though shallower by about half a magnitude. The full DES survey area will be ~ 35 times larger than that presented here, at roughly the same depth. The techniques and tools developed in this work will be applied to this new survey data, allowing significant expansion of the work here.

REFERENCES

Amara A. et al., 2012, MNRAS, 424, 553
Bacon D. J., Massey R. J., Refregier A. R., Ellis R. S., 2003, MNRAS, 344, 673
Bacon D. J., Refregier A. R., Ellis R. S., 2000, MNRAS, 318, 625
Bahcall N. A., Fan X., 1998, ApJ, 504, 1
Bartelmann M., Narayan R., Seitz S., Schneider P., 1996, ApJ, 464, L115
Bartelmann M., Schneider P., 2001, Physics Reports, 340, 291
Becker M. R., 2013, MNRAS, 435, 115
Benítez N., 2000, ApJ, 536, 571
Bergé J., Amara A., Réfrégier A., 2010, ApJ, 712, 992

Bertin E., 2006, in Astronomical Society of the Pacific Conference Series, Vol. 351, Astronomical Data Analysis Software and Systems XV, Gabriel C., Arviset C., Ponz D., Enrique S., eds., p. 112

Bertin E., 2011, in Astronomical Society of the Pacific Conference Series, Vol. 442, Astronomical Data Analysis Software and Systems XX, Evans I. N., Accomazzi A., Mink D. J., Rots A. H., eds., p. 435

Bertin E., Arnouts S., 1996, A&AS, 117, 393

Bertin E., Mellier Y., Radovich M., Missonnier G., Didelon P., Morin B., 2002, in Astronomical Society of the Pacific Conference Series, Vol. 281, Astronomical Data Analysis Software and Systems XI, Bohlender D. A., Durand D., Handley T. H., eds., p. 228

Bonnett C., 2013, ArXiv e-prints

Bridle S. L., Hobson M. P., Lasenby A. N., Saunders R., 1998, MNRAS, 299, 895

Bruzual G., Charlot S., 2003, MNRAS, 344, 1000

Busha M. T., Wechsler R. H., Becker M. R., Erickson B., Evrard A. E., 2013, in American Astronomical Society Meeting Abstracts, Vol. 221, American Astronomical Society Meeting Abstracts, p. 341.07

Coe D., Benítez N., Sánchez S. F., Jee M., Bouwens R., Ford H., 2006, AJ, 132, 926

Coleman G. D., Wu C.-C., Weedman D. W., 1980, ApJS, 43, 393

Conroy C., Wechsler R. H., Kravtsov A. V., 2006, ApJ, 647, 201

Crocce M., Pueblas S., Scoccimarro R., 2006, MNRAS, 373, 369

de Vaucouleurs G., 1948, Annales d'Astrophysique, 11, 247

Dempster A. P., Laird N. M., Rubin D. B., 1977, JOURNAL OF THE ROYAL STATISTICAL SOCIETY, SERIES B, 39, 1

Desai S. et al., 2012, ApJ, 757, 83

Diehl H. T. et al., 2014, in Society of Photo-Optical Instrumentation Engineers (SPIE) Conference Series, Vol. 9149, Society of Photo-Optical Instrumentation Engineers (SPIE) Conference Series, p. 0

Diehl H. T., Dark Energy Survey Collaboration, 2012, in American Astronomical Society Meeting Abstracts, Vol. 219, American Astronomical Society Meeting Abstracts 219, p. 413.05

Flaugher B., 2005, International Journal of Modern Physics A, 20, 3121

Flaugher B., The Dark Energy Survey Collaboration, submitted to A. J.

Flaugher B. L. et al., 2012, in Society of Photo-Optical Instrumentation Engineers (SPIE) Conference Series, Vol. 8446, Society of Photo-Optical Instrumentation Engineers (SPIE) Conference Series, p. 11

Fosalba P., Gaztañaga E., Castander F. J., Manera M., 2008, MNRAS, 391, 435

Fu L. et al., 2014, MNRAS, 441, 2725

Graff P., Feroz F., 2013, SkyNet: Neural network training tool for machine learning in astronomy. Astrophysics Source Code Library

Haiman Z., Mohr J. J., Holder G. P., 2001, ApJ, 553, 545

Heymans C. et al., 2008, MNRAS, 385, 1431

Heymans C. et al., 2012, MNRAS, 427, 146

Hinshaw G. et al., 2013, ApJS, 208, 19

Ho S. et al., 2012, ApJ, 761, 14

Hoekstra H., Jain B., 2008, Annual Review of Nuclear and Particle Science, 58, 99

Hoekstra H. et al., 2006, ApJ, 647, 116

Hogg D. W., Lang D., 2013, PASP, 125, 719

Holder G., Haiman Z., Mohr J. J., 2001, ApJ, 560, L111

Hwang H. S., Geller M. J., Diaferio A., Rines K. J., Zahid H. J., 2014, ApJ, 797, 106

Jain B., Khoury J., 2010, Annals of Physics, 325, 1479

Jain B., Van Waerbeke L., 2000, ApJ, 530, L1

Jarvis M., Jain B., Bernstein G., Dolney D., 2006, ApJ, 644, 71

Jauzac M. et al., 2012, MNRAS, 426, 3369

Jee M. J., Tyson J. A., Schneider M. D., Wittman D., Schmidt S., Hilbert S., 2013, ApJ, 765, 74

Kacprzak T., Zuntz J., Rowe B., Bridle S., Refregier A., Amara A., Voigt L., Hirsch M., 2012, MNRAS, 427, 2711

Kaiser N., Squires G., 1993, ApJ, 404, 441

Kaiser N., Wilson G., Luppino G. A., 2000, ArXiv Astrophysics e-prints

Kilbinger M. et al., 2013, MNRAS, 430, 2200

Kinney A. L., Calzetti D., Bohlin R. C., McQuade K., Storchi-Bergmann T., Schmitt H. R., 1996, ApJ, 467, 38

Knox L., Song Y.-S., Tyson J. A., 2006, Phys.Rev.D, 74, 023512

Kratochvil J. M., Haiman Z., May M., 2010, Phys.Rev.D, 81, 043519

Lewis A., Bridle S., 2002, Phys.Rev.D, 66, 103511

Lin H. et al., 2012, ApJ, 761, 15

Melchior P. et al., 2015, MNRAS, 449, 2219

Mohr J. J. et al., 2012, in Society of Photo-Optical Instrumentation Engineers (SPIE) Conference Series, Vol. 8451, Society of Photo-Optical Instrumentation Engineers (SPIE) Conference Series

Ngeow C. et al., 2006, in Society of Photo-Optical Instrumentation Engineers (SPIE) Conference Series, Vol. 6270, Society of Photo-Optical Instrumentation Engineers (SPIE) Conference Series, p. 23

Plionis M., Basilakos S., 2002, MNRAS, 330, 399

Reddick R. M., Wechsler R. H., Tinker J. L., Behroozi P. S., 2013, ApJ, 771, 30

Refregier A., Kacprzak T., Amara A., Bridle S., Rowe B., 2012, MNRAS, 425, 1951

Ross A. J. et al., 2012, MNRAS, 424, 564

Rykoff E. S. et al., 2012, ApJ, 746, 178

Rykoff E. S. et al., 2014, ApJ, 785, 104

Sánchez C. et al., 2014, MNRAS, 445, 1482

Semboloni E. et al., 2006, A&A, 452, 51

Sevilla I. et al., 2011, ArXiv e-prints

Shan H. Y. et al., 2014, MNRAS, 442, 2534

Sheldon E. S., 2014, MNRAS, 444, L25

Springel V., 2005, MNRAS, 364, 1105

The Dark Energy Survey Collaboration, 2005, ArXiv Astrophysics e-prints

Van Waerbeke L., 2000, MNRAS, 313, 524

Van Waerbeke L. et al., 2013, MNRAS, 433, 3373

Van Waerbeke L., Hinshaw G., Murray N., 2014, Phys.Rev.D, 89, 023508

Van Waerbeke L. et al., 2000, A&A, 358, 30

White M., van Waerbeke L., Mackey J., 2002, ApJ, 575, 640

Zuntz J., Kacprzak T., Voigt L., Hirsch M., Rowe B., Bridle S., 2013, MNRAS, 434, 1604

AFFILIATIONS

[1]Argonne National Laboratory, 9700 South Cass Avenue, Lemont, IL 60439, USA

[2]Department of Physics and Astronomy, University of Pennsylvania, Philadelphia, PA 19104, USA

[3]Department of Physics, ETH Zurich, Wolfgang-Pauli-Strasse 16, CH-8093 Zurich, Switzerland

[4]Institute of Cosmology & Gravitation, University of Portsmouth, Portsmouth, PO1 3FX, UK

[5]Department of Physics, Stanford University, 382 Via Pueblo Mall, Stanford, CA 94305, USA

[6]Kavli Institute for Particle Astrophysics & Cosmology, P. O. Box 2450, Stanford University, Stanford, CA 94305, USA

[7]Institut de Física d'Altes Energies, Universitat Autònoma de Barcelona, E-08193 Bellaterra, Barcelona, Spain

[8]Jodrell Bank Center for Astrophysics, School of Physics and Astronomy, University of Manchester, Oxford Road, Manchester, M13 9PL, UK

[9]Kavli Institute for Cosmological Physics, University of Chicago, Chicago, IL 60637, USA

[10]Fermi National Accelerator Laboratory, P. O. Box 500, Batavia, IL 60510, USA

[11]Institut de Ciències de l'Espai, IEEC-CSIC, Campus UAB, Facultat de Ciències, Torre C5 par-2, 08193 Bellaterra, Barcelona, Spain

[12]Department of Physics & Astronomy, University College London, Gower Street, London, WC1E 6BT, UK

[13]Center for Cosmology and Astro-Particle Physics, The Ohio State University, Columbus, OH 43210, USA

[14]Department of Physics, The Ohio State University, Columbus, OH 43210, USA

[15]University of Arizona, Department of Physics, 1118 E. Fourth St., Tucson, AZ 85721, USA

[16]SLAC National Accelerator Laboratory, Menlo Park, CA 94025, USA

[17]Brookhaven National Laboratory, Bldg 510, Upton, NY 11973, USA

[18]Cerro Tololo Inter-American Observatory, National Optical Astronomy Observatory, Casilla 603, La Serena, Chile

[19]Institute of Astronomy, University of Cambridge, Madingley Road, Cambridge CB3 0HA, UK

[20]Kavli Institute for Cosmology, University of Cambridge, Madingley Road, Cambridge CB3 0HA, UK

[21]Institut d'Astrophysique de Paris, Univ. Pierre et Marie Curie & CNRS UMR7095, F-75014 Paris, France

[22]Laboratório Interinstitucional de e-Astronomia - LIneA, Rua Gal. José Cristino 77, Rio de Janeiro, RJ - 20921-400, Brazil

[23]Observatório Nacional, Rua Gal. José Cristino 77, Rio de Janeiro, RJ - 20921-400, Brazil

[24]Department of Physics, University of Illinois, 1110 W. Green St., Urbana, IL 61801, USA

[25]National Center for Supercomputing Applications, 1205 West Clark St., Urbana, IL 61801, USA

[26]George P. and Cynthia Woods Mitchell Institute for Fundamental Physics and Astronomy, and Department of Physics and Astronomy, Texas A&M University, College Station, TX 77843, USA

[27]Department of Physics, Ludwig-Maximilians-Universitaet, Scheinerstr. 1, 81679 Muenchen, Germany

[28]Excellence Cluster Universe, Boltzmannstr. 2, 85748 Garching, Germany

[29]Robert Bosch LLC, 4009 Miranda Ave, Suite 225, Palo Alto, CA 94304, USA

[30]Department of Physics, University of Michigan, Ann Arbor, MI 48109, USA

[31]Max Planck Institute for Extraterrestrial Physics, Giessenbachstrasse, 85748 Garching, Germany

[32]University Observatory Munich, Scheinerstrasse 1, 81679 Munich, Germany

[33]Australian Astronomical Observatory, North Ryde, NSW 2113, Australia

[34]ICRA, Centro Brasileiro de Pesquisas Físicas, Rua Dr. Xavier Sigaud 150, CEP 22290-180, Rio de Janeiro, RJ, Brazil

[35]Department of Astronomy, University of Michigan, Ann Arbor, MI 48109, USA

[36]Institució Catalana de Recerca i Estudis Avançats, E-08010 Barcelona, Spain

[37]Jet Propulsion Laboratory, California Institute of Technology, 4800 Oak Grove Dr., Pasadena, CA 91109, USA

[38]Department of Physics and Astronomy, Pevensey Building, University of Sussex, Brighton, BN1 9QH, UK

[39]Centro de Investigaciones Energéticas, Medioambientales y Tecnológicas (CIEMAT), Madrid, Spain

[40]SEPnet, South East Physics Network, (www.sepnet.ac.uk)

APPENDIX A: FOREGROUND SAMPLE SELECTION

As discussed in §3.2, we consider two factors that can affect the selection of our foreground sample – spatial variation in depth and spatial variation in seeing. If not taken care of, these effects will result in apparent spatial variation of the foreground galaxy number density that is not due to the cosmological clustering of galaxies. Below we describe tests for each of these and determine a set of selection criteria based on the analysis.

A1 Depth variation

Spatial variation in the depth of the images can cause the apparent galaxy number density to vary, as more or less galaxies survive the detection threshold. We would like to construct a foreground galaxy sample which minimizes this varying depth effect. A simple solution is to place a magnitude cut slightly shallower than the limiting magnitude in all of the areas considered, so that the sample is close to complete in that magnitude range.

We find that in our area of interest, with a magnitude cut at $i < 22$, we have 97.5% of the area that is complete to this magnitude limit[6], while the 2.5% slightly shallower is not expected to yield significant change in our results.

A2 Seeing variation

Spatial variation in seeing can lead to spatial variation in apparent galaxy number density, as large seeing leads to less effective star-galaxy separation as well as higher probability of blending in crowded fields. To test this, we first select a foreground sample with $i < 22$ and $0.1 < z < 0.5$ according to §3.2. Then we look at the correlation between the galaxy number density in this foreground sample and the average seeing values at these locations, both calculated on a grid of 5×5 arcmin^2 pixels without smoothing. Figure A1 shows the galaxy number density versus seeing. The black data points show the mean and RMS (multiplied by 10 for easy visualisation) of the scatter plot in 15 seeing bins. There is a small anti-correlation between these two values at the 6% level. This is at an acceptable level for us to continue the analysis without masking out the extreme high/low seeing regions.

---

[6] Note that we use the 10σ galaxy limiting magnitude, which is a rather conservative measure for the completeness, as we detect many more galaxies below 10σ. Those galaxies would be complete at fainter magnitude cuts.
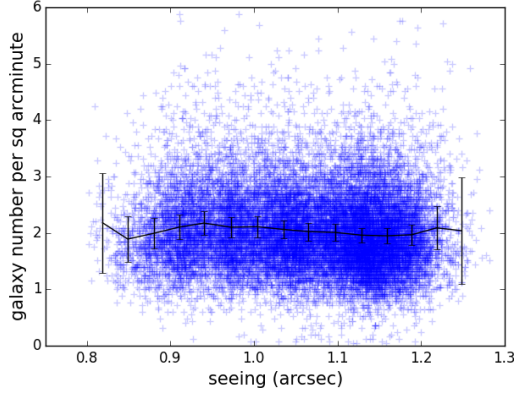
Figure A1. Galaxy number density as a function of the seeing in the area of consideration. The black line shows the mean and RMS (multiplied by 10 for easy visualisation) of the scatter plot in 15 seeing bins.

APPENDIX B: CORRECTING FOR SYSTEMATIC CONTAMINATION USING PCA

As shown in §6, we can use Eqn. 18 to check for any outstanding systematic contamination in our κ_E map and its correlation with the κ_g map. Here we present a general treatment to correct for these systematic contaminations, similar to that used in Ross et al. (2012) and Ho et al. (2012).

Assume that our measured κ_E map is a linear combination of the true $\kappa_{E,\text{true}}$ map and some small coefficient α_i times the systematics maps $\{M_i\}$ that can potentially contaminate the κ_E maps (*e.g.* seeing, PSF ellipticity). That is

$$\kappa_E = \kappa_{E,\text{true}} + \sum_i^N \alpha_i M_i, \tag{B1}$$

where we have a total of N systematics maps. Similarly, we have the expression for the measured κ_g in the same way

$$\kappa_g = \kappa_{g,\text{true}} + \sum_i^N \beta_i M_i, \tag{B2}$$

where β_i is the linear coefficient in this case.

Assuming the true maps are uncorrelated with the systematics maps, we have

$$\langle \kappa_{E,\text{true}} M_i \rangle = 0; \tag{B3}$$

$$\langle \kappa_{g,\text{true}} M_i \rangle = 0. \tag{B4}$$

Correlating the measured κ_E with a single systematics map gives

$$\langle \kappa_E M_j \rangle = \langle (\sum_i^N \alpha_i M_i) M_j \rangle. \tag{B5}$$

We can construct a set of systematics maps that are uncorrelated between each other, or $\langle M_i M_{j \neq i} \rangle = 0$, and then extract all the coefficients α_i from the observables as follows:

$$\langle \kappa_E M_j \rangle = \alpha_j \langle M_j M_j \rangle;$$

$$\alpha_j = \frac{\langle \kappa_E M_j \rangle}{\langle M_j M_j \rangle};$$

$$\kappa_{E,\text{true}} = \kappa_E - \sum_i^N \frac{\langle \kappa_E M_i \rangle}{\langle M_i M_i \rangle} M_i. \tag{B6}$$
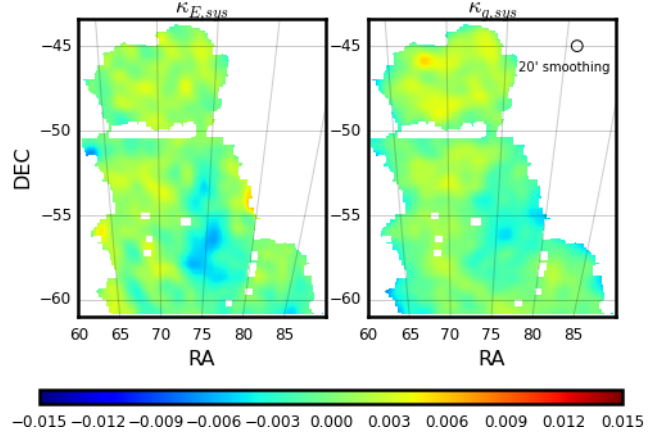

Figure B1. The systematics map for κ_E (left) and κ_g (right) shown is compiled using a linear combination of 20 principal components extracted from the systematics maps listed in Table 2.

And similarly for κ_g, we have

$$\kappa_{g,\text{true}} = \kappa_g - \sum_i^N \frac{\langle \kappa_g M_i \rangle}{\langle M_i M_i \rangle} M_i. \tag{B7}$$

To construct a set of systematics maps $\{M_i\}$ uncorrelated between each other from a set of systematics maps correlated with each other $\{M'_i\}$ (*i.e.* those listed in Table 2), we invoke the Principal Component Analysis (PCA) method. In this case, each of the pixelated maps, after normalizing by its scatter, $\{M'_i\}$ form a data vector, and the extracted eigenvectors form a orthogonal basis set, which we can use as $\{M_i\}$. We find that the principal component maps correspond strikingly to physical properties of the data. Figure B1 shows the systematics maps corresponding to κ_E and main sample κ_g extracted using this PCA method, or the second terms on the right-hand-size of Equation B6 and Equation B7. We find that the main contributions come from large-scale structures and are at a very low level compared to the original maps (see Figure 2). We subtract these systematics maps from the original κ_E and κ_g maps according to Eqn. B6 and Eqn. B7. The Pearson correlation coefficient changes by 3.5% relative to the original $\rho_{\kappa_E \kappa_g}$ measured in §5, suggesting the contamination to the cross-correlation coefficient is not significant.

It is worth noting that there are a few assumptions that go into the calculation above, which need to be accounted for when interpreting these results. First, we have assumed that the systematic maps have no correlation with the true κ_E and κ_g maps. For a large enough area, this should be true, but for small maps we can expect some correlation just by chance. Hence the quantitative "improvement" we get in the Pearson correlation coefficient must be carefully checked with simulations with larger area than used here. Second, since the method is based on PCA, the effectiveness of the correction depends on finding the important systematics maps that can contribute *linearly* to the contamination. That is, if the systematics come from a non-linear combination of the various maps (*e.g.* multiplication of two maps), then one would not automatically correct for it without putting in this correct non-linear combination of maps in the first place.